High power electrostatic beam splitter for a proton beamline

M. Hartmann,* D. Reggiani, J. Snuverink, H. Zhang, and M. Seidel†
Paul Scherrer Institut, Villigen, Switzerland

(Received 12 September 2023; accepted 26 January 2024; published 20 February 2024)

The High Intensity Proton Accelerator facility (HIPA) delivers a 590 MeV cw (50.6 MHz) proton beam with up to 1.4 MW beam power (2.4 mA) to spallation and meson production targets serving particle physics experiments and material research. The main accelerator is the ring cyclotron, an isochronous proton machine accelerating an injected 72 MeV beam to a final 590 MeV. A few meters downstream of the ring cyclotron, an electrostatic beam splitter was installed in the 1980s and originally designed to peel off from a 200 μA beam up to 20 μA (12 kW beam power). Future initiatives will also make use of the splitter. Specifically, as part of the Isotope and Muon Production using Advanced Cyclotron and Target technologies (IMPACT) upgrade project, Targeted Alpha Tumour Therapy and Other Oncological Solutions (TATTOOS), an online isotope separation facility will allow to produce promising radionuclides for diagnosis and therapy of cancer in quantities sufficient for clinical studies. The TATTOOS facility includes a dedicated beamline intended to operate at a beam intensity of 100 μA (60 kW beam power), requiring continuous splitting of the high-power main beam via the splitter. As a step forward toward reaching the desired beam intensity, a beam study was carried out to test the viability of the existing splitter for TATTOOS. The results of this study show that a record of 90 μA (53 kW beam power) was peeled off a horizontally and vertically enlarged beam by the splitter. The successful beam strategy employed during the study as well as the results of several key measurements are presented in this paper, with particular emphasis on diagnostic measurements. Additionally, to support the measurements, a computational model of the splitter has been implemented using Monte Carlo simulation tools, including realistic geometry, electrostatic fields, beam optics, and power deposition calculations. Overall, the results of this paper show that through the combination of beam measurements and simulations, the existing splitter can be used to reach the 100-μA beam intensity requirement for TATTOOS.

DOI: 10.1103/PhysRevAccelBeams.27.023502

I. INTRODUCTION

Since its operation in 1974, the HIPA facility, originally designed for a maximum beam current of 100 μA, has continuously been improved to reach a maximum average power of up to 1.4 MW (2.4 mA) at present [1]. The beam energy is increased via three accelerators connected in series. Protons are preaccelerated to 0.87 MeV by a Cockcroft-Walton dc linear accelerator and delivered through a transfer section to a 72 MeV injector cyclotron (injector II). The medium energy beam is then transported to the ring cyclotron that accelerates the protons further to 590 MeV [2]. After extraction from the ring cyclotron (extraction efficiency better than 99.98% [1]), the beam is delivered to several user facilities and experimental stations. The beam feeds two meson production targets, target M and target E, through a dedicated beamline (PK1), along with two spallation targets for thermal/cold neutrons (SINQ) and ultracold neutrons (UCN) [3]. In addition, a facility producing novel radionuclides for positron emission tomography (PET), the IP2 irradiation station [4], receives the 72 MeV beam from injector II parasitically. To meet the IP2 requirements, it is necessary to peel off a few tens of microamperes from the main 72 MeV (2.4 mA) beam via an electrostatic beam splitter (EXT) [5,6]. Similar to the EXT, another electrostatic beam splitter called EHT [7,8] in the PK1 beamline was originally designed in the 1980s to provide simultaneously a 200 μA proton beam to the meson production targets and to peel off up to 20 μA to the experimental and medical proton irradiation facilities [8]. The EHT splitter in particular is the primary focus of this paper. The layout of the HIPA complex [9] is illustrated in Fig. 1 where the relative locations of the electrostatic beam splitters are highlighted.

*marco.hartmann@psi.ch
Also at École Polytechnique Fédérale de Lausanne (EPFL), Lausanne, Switzerland.
†Also at École Polytechnique Fédérale de Lausanne (EPFL), Lausanne, Switzerland.

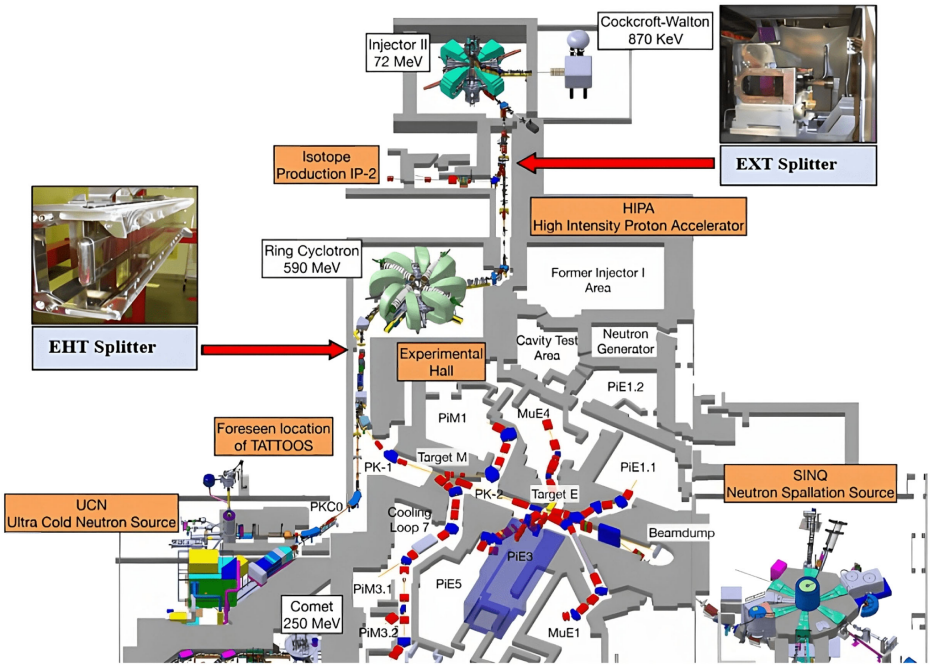

FIG. 1. Layout of the present state HIPA facility.

Future initiatives at PSI will also make use of electrostatic beam splitters allowing HIPA to remain at the forefront of intensity frontier research. In particular, as part of the upgrade project Isotope and Muon Production using Advanced Cyclotron and Target technologies (IMPACT) [9], a new radioisotope target station, Targeted alpha tumor therapy and other oncological solutions (TATTOOS) will enable the production and delivery of radionuclides for diagnosis and therapy of cancer in doses sufficient for clinical studies [10]. The TATTOOS beamline is intended to operate at a beam intensity of 100 μA (60 kW beam power), requiring continuous splitting of the high-powered beam [11] via the EHT. Due to the seldom use of the latter during HIPA operation and a beam intensity higher than originally designed for, it was uncertain whether the desired beam intensity for TATTOOS could be attained with the existing EHT. As reaching this intensity is a major requirement for TATTOOS, a recent beam study was carried out. The results of the study show that a record of 90 μA (53 kW beam power) was peeled off a horizontally and vertically enlarged beam by the EHT and sent to the UCN target, confirming the validity of the existing EHT for TATTOOS. The successful strategy employed in the beam study as well as the results of several key measurements are presented in this paper. Particular emphasis is placed on beam profile and diagnostic measurements. Besides beam measurements, simulations are essential to accelerator physics research, providing a means to study components and beamlines. In this regard, another aim of this paper is to benchmark realistic BDSIM/GEANT4 simulations [12–15] of the EHT against some of its measured characteristics, making use of the powerful interplay between geometrical considerations, electrostatic fields, beam optics, and Monte Carlo calculations.

Before discussing the measurement methodology (Sec. III) and the simulation model (Sec. IV), a description of the EHT is given including construction and operational details (Sec. II). An insight into the challenges of high-power electrostatic beam splitters is presented with a particular focus on the EHT.

II. EHT BEAM SPLITTER

A. Motivation

For both the IP2 and the UCN beamlines, the choice of using electrostatic beam splitters to peel off a portion of the full intensity beam (henceforth named main beam), rested on the fulfilment of four requirements [7]: (i) The time structure [50.6 MHz, 0.4 ns (FWHM)] of the main beam should be preserved. (ii) The beam intensity should be variable between zero and the maximum split intensity. (iii) The operation of providing beam for the respective facilities should not disturb the alignment of the main beam (i.e., an ideally homogenous field is required in one region for deflecting the beam and a low fringe field next to the septum of the splitter). (iv) The activation of the splitter itself and other beam transport components further downstream should be kept as low as possible.

These conditions excluded all rf splitting devices and left systems with magnetic or electrostatic septa. Since in practice, the performance of the high energy HIPA beamlines is limited by the beam losses [16], electrostatic beam

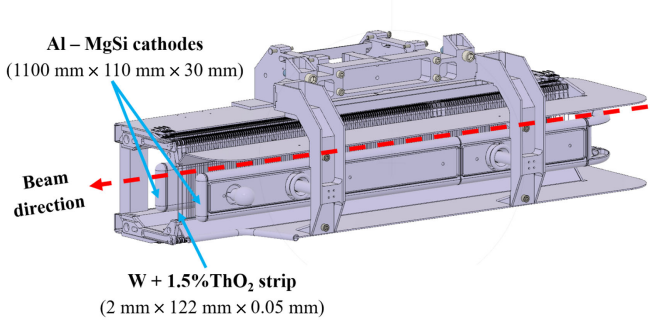

FIG. 2. Computer aided design (CAD) of the EHT splitter.

splitters with their thin septum (septum thickness ≤100 μm) were chosen due to lower expected losses [17].

B. Design description

The limitation in space to introduce the EHT in the PK1 beamline, excluded single sided septa that require significantly high voltages to produce the required beam deflection [7]. By applying a field on both sides of a thin septum, the voltage specifications could be met. Indeed, the EHT (Fig. 2) consists of two aluminium (Al-MgSi) cathodes (1100 mm long, 110 mm high, and 30 mm thick) at a fixed voltage of −172 kV and a thin septum. Both cathodes and septum are movable. The septum (1094 mm long) is located equidistant from the cathodes at 60 mm and consists of 175 tungsten alloy (W + 1.5% ThO_2) strips. Each strip is 2 mm long, 122 mm high, and 0.05 mm thick and separately tensioned at 10 kg/mm^2 by a pair of strings such that if a strip breaks, the tensioning springs pull the fragments into upper and lower storage containers outside of the beam path. Gaps along the septum are present to accommodate for several pickups measuring the current on the strips. The gaps between the first four, the last four, and the 55th–58th strips counting from the entrance side are 10 mm while all other gaps are 4 mm.

C. Layout and operation

A sketch of the PK1 (from the upstream end of the first bending magnet after the ring cyclotron, the so-called AHA bending magnet, to the entrance of target M) and UCN beamlines is displayed in Fig. 3 with the EHT region and profile monitors highlighted. The two cathodes of the EHT, create two symmetric electric fields on every side of the strips that are on ground potential (the net electric force acting on the strips is always zero). The incoming protons of the main beam are thus steered away by 3 mrad from the strips at the end of the splitter for each beam. Two identical steering magnets called SHC4X on each side of the EHT compensate for the effect of the electrostatic field on the main beam and increase the deflection of the split beam such that the former beam has no deflection while the latter beam has a total horizontal deflection of 6 mrad at the exit of the second SHC4X magnet (Fig. 4). Further downstream, a septum magnet (about 8 m downstream of the EHT) called ABS diverts the split beam toward the UCN beamline and target. The main beam may also be directed from targets M, E, and SINQ to the UCN beamline via a fast kicker magnet installed in front of the EHT. Importantly, the fast kicker magnet and EHT cannot

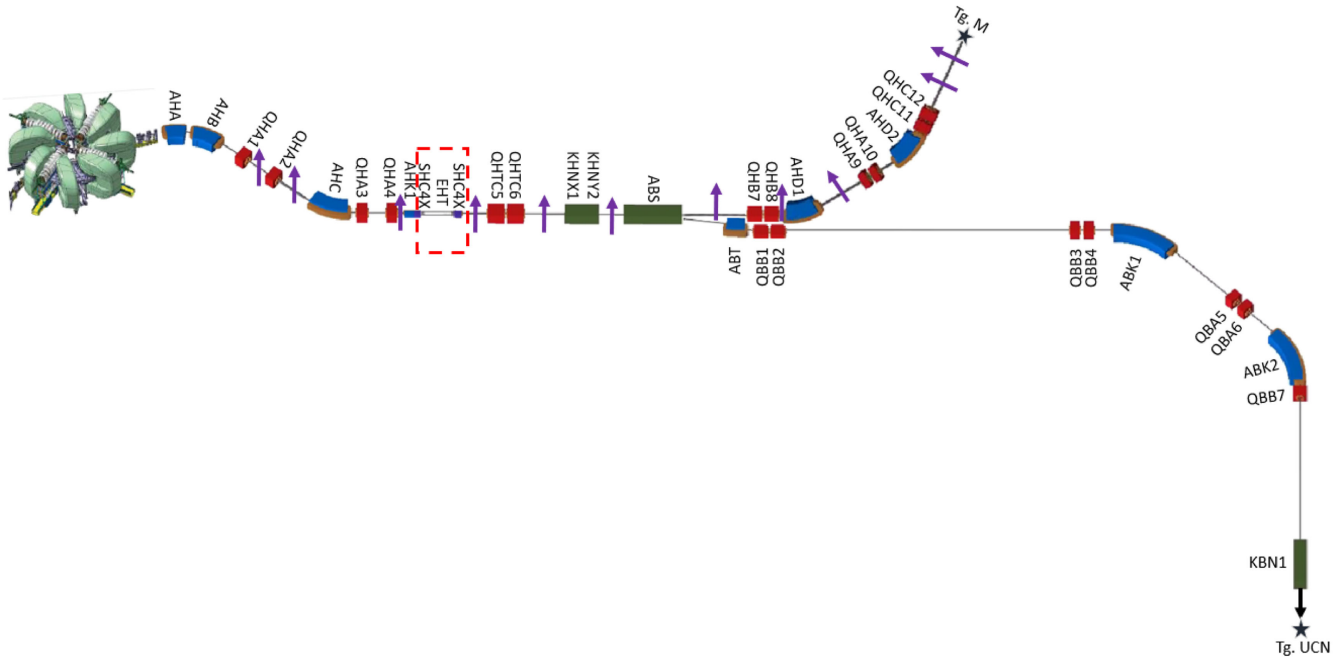

FIG. 3. BDSIM model of the PK1 and UCN beamlines. The EHT region is located approximately 12 m downstream of the AHA dipole and highlighted in a dashed red box. The profile (horizontal and vertical) monitors in the PK1 beamline are marked with purple arrows.

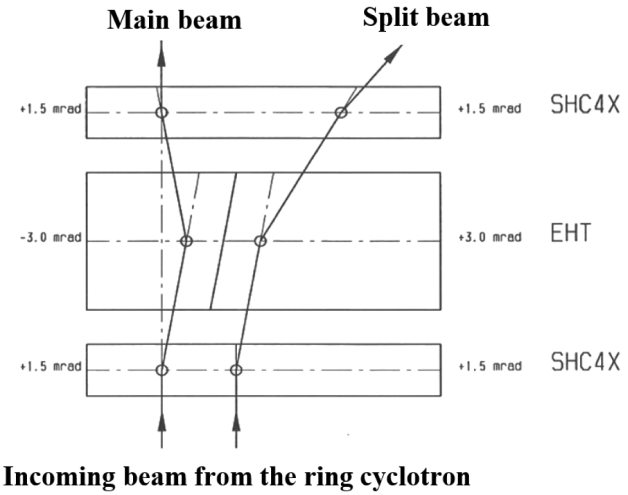

FIG. 4. Combined action of EHT splitter and two SHC4X magnets. The incoming beam is split into two beams (main and split beams) that follow the trajectories marked by arrows.

operate simultaneously (see Sec. III A for details on UCN operational modes).

With regard to operational safety, the handling of the EHT is done remotely in order to reduce the exposure to service personnel. When the splitter is lowered, the cathodes self-connect to a flexible high-voltage coupler. The HV applied to the cathodes and the current of the steering magnets are not varied during operation providing a significant advantage since there is no HV deconditioning. A detailed description of the EHT vacuum chamber is provided in [8].

Finally, the split beam intensity can be regulated by moving the whole device in the horizontal x plane (with z the longitudinal beam direction and y the vertical plane) such that the strips are more into the central region of the beam distribution (see Sec. III C). This is accomplished via a high precision gear system coupled to two rails with dc motors that position the septum to better than 0.1 mm. With an offset in the positioning on the two rails, the EHT's rotation angle relative to the incoming beam can be adjusted allowing to minimize the power deposited on its septum (see Sec. IV E). The relative precision of the EHT's rotation angle is about 10 μrad.

D. Challenges of the high-power EHT splitter

Several upgrades of the EHT starting from the late 1990s occurred to face the challenges of the increasing HIPA beam power. Power deposition and showers of secondary particles are induced when the high-power beam is brought into contact with accelerator components. In this regard, one challenge concerning the EHT is the activation generated by head-on proton collisions of the beam with the septum, as stated in [8] and [18]. These protons undergo angular scattering and are lost downstream along the beamline (see [7] and [11] for a qualitative description of the scattering processes occurring on the strips). The angular scattering distribution of the protons depends principally on the septum material and the distribution along the beam axis. In particular, the septum can be made either of wires or strips of different dimensions. Monte Carlo simulations have shown that for a septum composed of thin wires, the angular distribution of scattered protons is narrower compared to one composed of strips [18]. In this case, the protons scatter as far off as the vacuum tube of the ABK1 bending magnet (about 30 m distant from the EHT). However, if the angular distribution is broad (i.e., a septum consisting of strips), most protons are lost in the neighborhood of the EHT (before the ABS septum magnet). For this reason, starting from the 1998 shutdown period of the accelerator, operation was continued with the "strip" version of the EHT septum since it is easier to shield and radiation-harden the EHT-ABS region of the PK1 beamline instead of the remaining regions further downstream. In addition, to further limit the beam losses in the EHT-ABS region, two copper collimators KHNX1 and KHNY2 (located approximately 4.7 m and 5.3 m downstream of the EHT, respectively) with movable jaws act as absorbers by reducing the horizontal (respectively vertical) beam halo of both main and split beams (see [11] for parametric studies on the apertures of each collimator to reduce the power deposited downstream of the EHT).

The large power deposition on the strips of the EHT itself (especially on the first strip, see Sec. IV F) is also a major challenge. Since the splitting action of the EHT is restricted to the horizontal plane, the power deposited on the strips can be decreased if the horizontal width of the main beam is made broader. In this way, the power density seen by the strips of the septum is lower, while the extracted intensity is the same. Likewise, increasing the vertical main beam width is beneficial since this will spread the power deposition along the strips. Indeed, previous simulations in this direction [19,20] have shown that increasing the beam width horizontally by 30% with respect to the nominal beam size with the same focusing on target M results in a 33% lower power deposition (with 100 μA split-off from 2 mA) on the first strip of the EHT without significantly increasing the losses downstream in the PK1 beamline. Following the results of these simulations, a beam study was devised where the EHT was operated with different horizontally and vertically enlarged optics. The procedure as well as the results of the study are described in detail in the following section.

III. EHT BEAM STUDY

A. Measurement procedure and beam optics

As mentioned in Sec. II C, the full intensity proton beam from the ring cyclotron may be steered onto the spallation target of the UCN source. This can be achieved using two

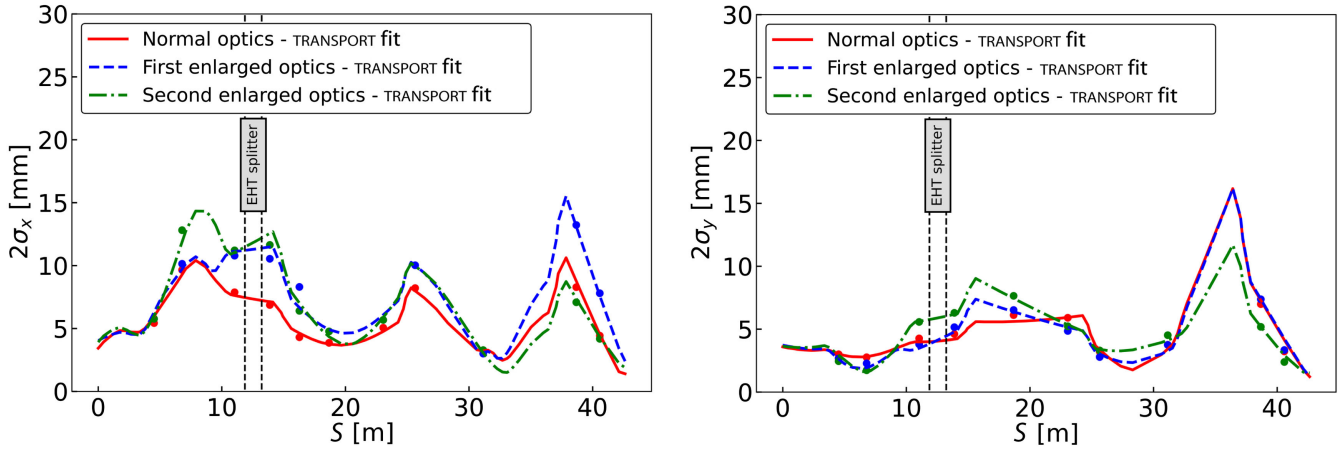

FIG. 5. Measured horizontal (left) and vertical (right) beam widths with TRANSPORT envelope fits from the upstream end of the AHA bending magnet to the entrance of target M. The measured beam widths are marked with dots. The position of the EHT splitter is marked with dashed vertical lines.

mutually exclusive modes [21]: (i) Pulsed beam mode: A fast kicker magnet (rise time of 0.5 ms [22]) is used to divert the beam from targets M and E and SINQ to UCN, typically every 5 min for 8 s. This corresponds to a duty cycle of approximately 3%. Before the beam is switched back to the meson production and SINQ targets, the beam current is lowered to about 1.2 mA and then raised to the maximum again within 20 s. This is done to avoid high stress to the targets, especially the SINQ target [1]. (ii) Splitter mode: It is possible to operate the EHT to shear off a fraction of the main beam and send it continuously to the UCN target.

The two modes produce an angular deviation of 6 mrad and a horizontal displacement of about 40 mm at the position of the ABS septum, which is necessary to deflect the beam into the UCN beamline.

Due to its prevalent historical application for simulating the HIPA proton channel, TRANSPORT [23,24], was employed to determine the initial beam conditions at the extraction of the ring cyclotron that match the measured beam widths up to target M. This allowed three beam optics—one nominal ("normal"), one horizontally enlarged ("first enlarged"), and one horizontally and vertically enlarged ("second enlarged") to be tested with the UCN splitter mode. The resulting split beam intensity was measured for all three optics by a beam current monitor located upstream of the ABK1 dipole magnet in the UCN beamline. Besides the splitter mode, it was also verified that the pulsed beam mode is feasible with enlarged optics. The measured beam widths and the TRANSPORT envelope fits for all three optics tested are illustrated in Fig. 5, while the simulated beam ellipses before the EHT are shown in Fig. 6. It can be seen that the beam is widened at the EHT location and that the particle density hitting the strip is lower for the enlarged optics.

Likewise, Table I indicates the horizontal and vertical beam sizes at the entrance of the EHT from TRANSPORT for

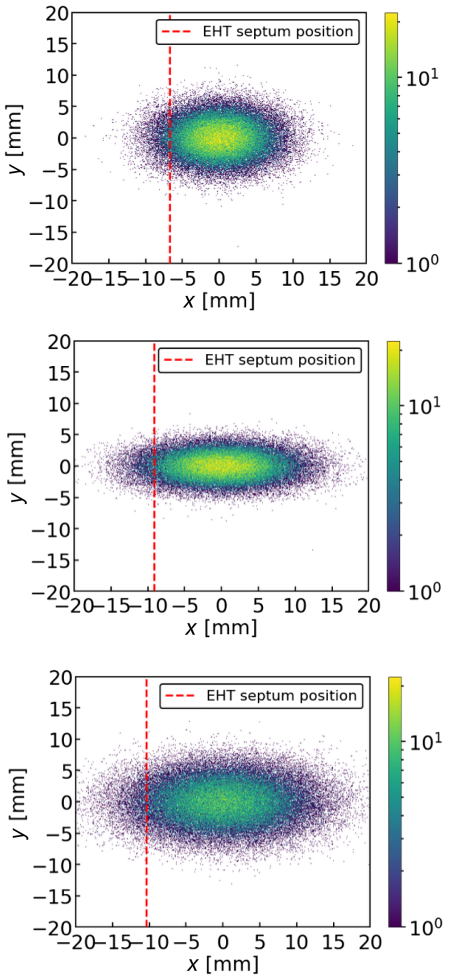

FIG. 6. Simulated BDSIM beam ellipses for the tested normal optics (top), first enlarged optics (middle), and second enlarged optics (bottom). The position of the EHT septum corresponding to a split current of 80 μA is marked with a dashed red line for each optics.

TABLE I. Beam sizes from TRANSPORT fits at the entrance of the EHT and split current achieved with UCN splitter mode.

Optics tested	$2\sigma_x$ (mm)	$2\sigma_y$ (mm)	Split beam current (μA)	Stability of split beam current (%)	Main beam current (mA)
Normal	7.5	4.8	62	4.0	1.8
First enlarged	10.4	3.7	87	2.9	1.4
Second enlarged	12.3	6.0	90	2.4	1.4

the three different optics. With regard to the measurement of split beam current, a calibration error was found on the current monitor and subsequently taken into account using a curve fitting method (see Sec. III C). The values of split beam current after recalibration are reported in Table I for each optics as well as the stability of the split beam. It is equally worth noting that the beam current from the ring cyclotron was different for the three optics, namely 1.8 mA for the normal optics and 1.4 mA for the enlarged optics. As several key quantities related to the EHT depend on the beam current at extraction, the proton beam from the ring cyclotron is first characterized in Sec. III B.

Finally, the beam losses after the EHT were measured by ionization chambers placed close to the splitter and at other positions further downstream. Several control parameters were optimized to reduce the losses, these included: the aperture of the two collimators KHNX1 and KHNY2, the rotation angle of the EHT to reduce the power deposition on the septum (see Sec. IV E), and the horizontal position of the ABS septum magnet relative to the beam.

B. Proton beam at extraction

Since the amount of split beam current is related to the horizontal width of the main beam, which itself is dependent on the beam current at extraction, it is important to characterize the proton beam from the ring cyclotron for all three optics. In general, in isochronous cyclotrons like the ring cyclotron, it is well known from simulations and measurements that the beam size can be described with a quartic dependency on the beam current [25–27]. Typically, at beam currents of 0.5 mA and above, the following equation is used to approximate the beam size at extraction [28]:

$$\frac{\sigma_{x0}(I)}{\sigma_{x0}(I_{\mathrm{ref}})} = \left(\frac{I}{I_{\mathrm{ref}}}\right)^{1/4}, \tag{1}$$

where I_{ref} is the beam current taken at 1 mA. An equation of the same form as Eq. (1) can be applied to the vertical plane.

In this framework, beam widths during the study were directly measured with wire scanners for currents between 0.1 and 1.8 mA for all three optics tested (Fig. 7). Evidently, Eq. (1) is valid for the range of beam currents measured, allowing a fair comparison of the beam sizes to be made for all three optics.

C. Power deposition on second strip

In an attempt to understand the power deposited on the EHT, the current of the colliding protons with the strips of the septum is measured with current pickups for the first three strips. However, no signal was detected on the first strip which indicates that this strip was either broken (before our experiments) or that the measurement itself is defect. It is assumed that the measurement on the second strip pertains in fact to the first strip. Nevertheless, if the measurement relates to the second strip, the reasoning and conclusions are still valid.

The measured average uncalibrated current on the second strip as a function of average split current for all three optics tested is illustrated in Fig. 8. In order to select data points under stable beam conditions, the data (collected over a period of 12 and 8 h runs on two consecutive days) were binned in intervals of 400 ms, averaged, and used in the analysis if the coefficient of variation (CV) of four quantities (main beam current, split beam current, current on the second strip, and EHT position) was less than 10%. To ensure safe operation for all three optics, an upper operation limit was set for the current on the strip from experience with the EXT of the IP2 beamline. The power

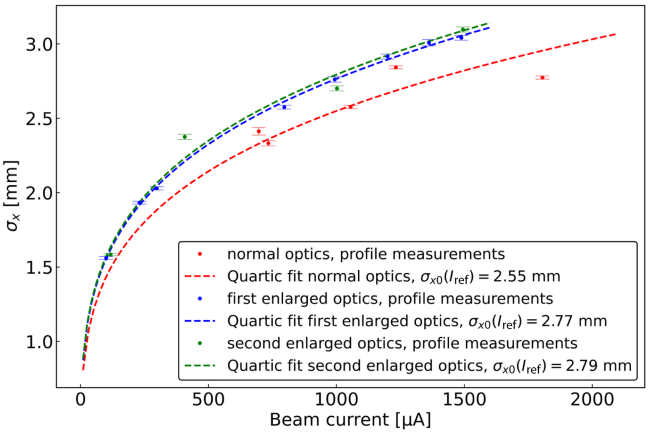

FIG. 7. Horizontal beam size versus beam current approximately 4.5 m after extraction and after the first quadrupoles (QHA1 and QHA2) in the PK1 beamline.

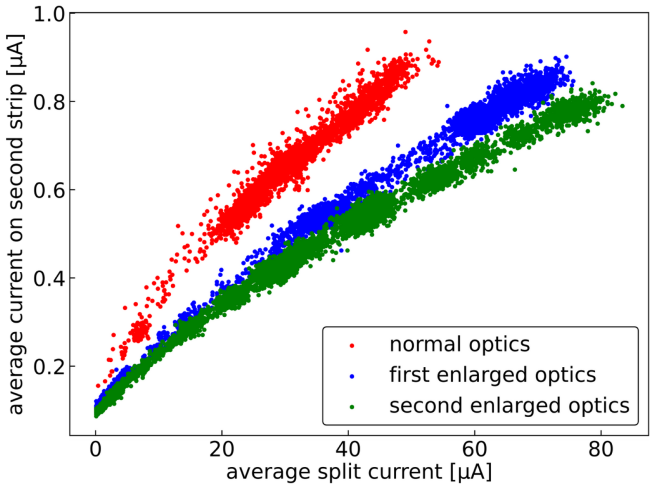

FIG. 8. Measured average current on second strip versus uncalibrated average split current.

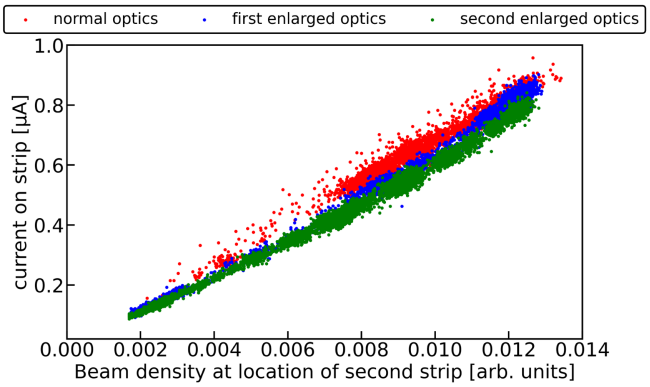

FIG. 9. Relationship between measured current on the second strip and beam density at the location of the second strip.

deposit that is deemed safe for the EXT splitter is equivalent to 50 μA split current for the EHT splitter with normal optics [29]. With normal optics the measured current on the second strip was 0.9 μA. Therefore, this upper limit was taken for all three optics, and indeed, no strip has been broken.

As mentioned in Sec. III A and as can be seen in Fig. 8, a calibration offset exists in the measured average split current. The reason for this is that the slope of the current monitor (a Faraday cup) is typically calibrated at high current (pulsed beam mode) only. To account for this offset, all three curves in Fig. 8 are fitted with a third order polynomial as this shows good matching with the measured data. The zeros of the polynomial fits correspond to the current offset. The three fits show that the current is underestimated by an average of 6.5 μA. The calibrated split beam currents are indicated in Table I.

The current on a strip, like the amount of split beam current, is related to the horizontal profile of the main beam. To clarify this dependency, a method was established for all three optics based on the following reasoning. First, at the EHT, the shape of the main beam can be described by Gaussian distributions in both horizontal and vertical directions (see Sec. IV C). Moving the strips of the septum toward the center of the beam profile increases the amount of split beam current as well as the current signal on the second strip (as shown in Fig. 8). By doing so, the local beam density also increases as a larger percentage of protons come into contact with the strip (i.e., the power deposited on the strip increases). This suggests that the current signal is related to the beam density at the location of the strip and to the power deposited on it. In order to verify this hypothesis, the horizontal main beam profiles at the EHT are first normalized for all three optics to account for the different beam currents measured at extraction. Subsequently, a look-up table is produced allowing to find the beam density at the location of the second strip for a given measured split beam current (with recalibration taken into account). A positive linear correlation between current on a strip and beam density is found, supporting the hypothesis (Fig. 9).

Finally, from Figs. 8 and 9, it can be confirmed that the power deposited on the strip is reduced with enlarged optics compared to normal optics, as expected.

D. Beam loss measurements

In order to study the beam losses and for the machine protection system, ionization chambers are placed close to the EHT (Fig. 10) and at other positions further downstream in the PK1 beamline (Fig. 11). As expected, a positive correlation exists between the power deposited on the strips and the losses in the vicinity of the EHT. Also here it can be seen that the enlarged optics are advantageous since by reducing the power deposit on the strips the ensuing beam losses are reduced. However, further

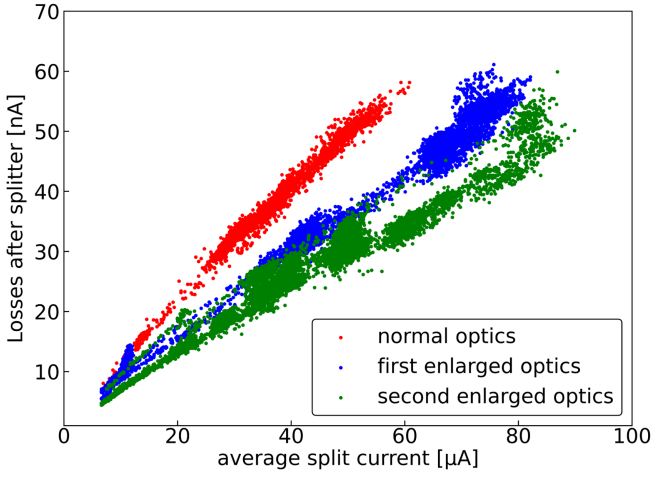

FIG. 10. Losses at ionization chamber MHI4 (about 2.3 m downstream of the EHT) versus average split current.

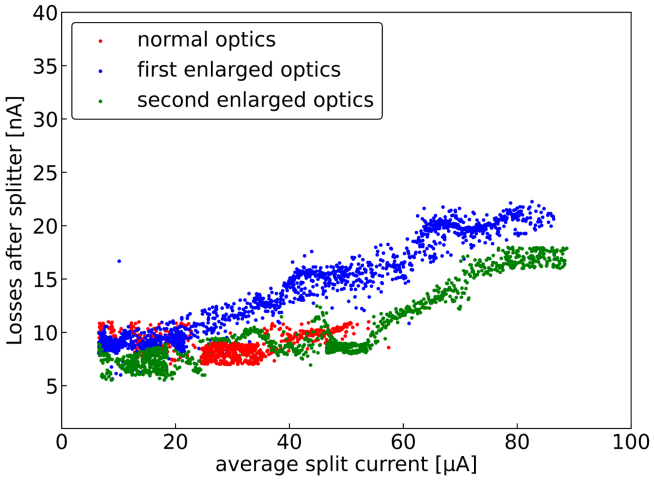

FIG. 11. Losses at ionization chamber MHI9 (about 17.9 m and 11.1 m downstream of the EHT and ABS respectively) versus average split current.

downstream, after the ABS, the correlation is lost as the particles constituting the halo of the main and split beams are absorbed by the horizontal (KHNX1) and vertical (KHNY2) collimators. The tuning of the collimator apertures is particularly effective for the normal beam optics where the losses remain approximately constant with increasing split beam current. However, for enlarged optics, an increase of the losses is observed. Although from the radiation protection point-of-view the beam losses are below the machine interlock limits, it is expected that additional tuning will further reduce the losses.

Overall, the diagnostic measurements outlined above show that enlarging the beam optics in the horizontal and vertical plane is beneficial to reduce not only the power deposited on the strips of the septum but also the beam losses a few meters downstream of the EHT.

E. Foreseen beam optics

Using the tested beam optics, a maximum of 90 μA intensity was peeled off a 63% horizontally and 24% vertically enlarged beam by the EHT. During the beam study, the capacity to enlarge the beam optics further was limited by the current on the magnetic coils of the PK1 quadrupoles. Upcoming beam studies with water cooled quadrupoles are planned and will allow to test more enlarged beam optics and to reach higher split beam intensities accordingly. Specifically, it is expected that by enlarging the beam horizontally and vertically by 70% and 40%, respectively (Fig. 12), the EHT could peel off approximately over 150 μA. This extracted intensity would be sufficient to operate TATTOOS. It is expected that enlarging the beam even further would not be advantageous as it would result in increased beam losses further downstream of the EHT, thereby limiting operational feasibility.

IV. SIMULATION MODEL

The challenges concerning the EHT beam splitter prompted the need to perform realistic tracking simulations in electromagnetic fields and accurately predict the complex interaction processes between the high-power proton beam and the strips of the EHT septum. Such simulations may be used to infer primary beam losses on the strips themselves as well as the subsequent production of secondary particles. In addition, tracking particle distributions in a sequence of elements with various magnetic fields allows to verify the beam optics of the PK1 beamline, which is crucial for our analysis. For these reasons, Monte Carlo simulation tools were selected to build a robust simulation model of the PK1 beamline, including the EHT. In the following section, the most important characteristics of the EHT are studied via simulations.

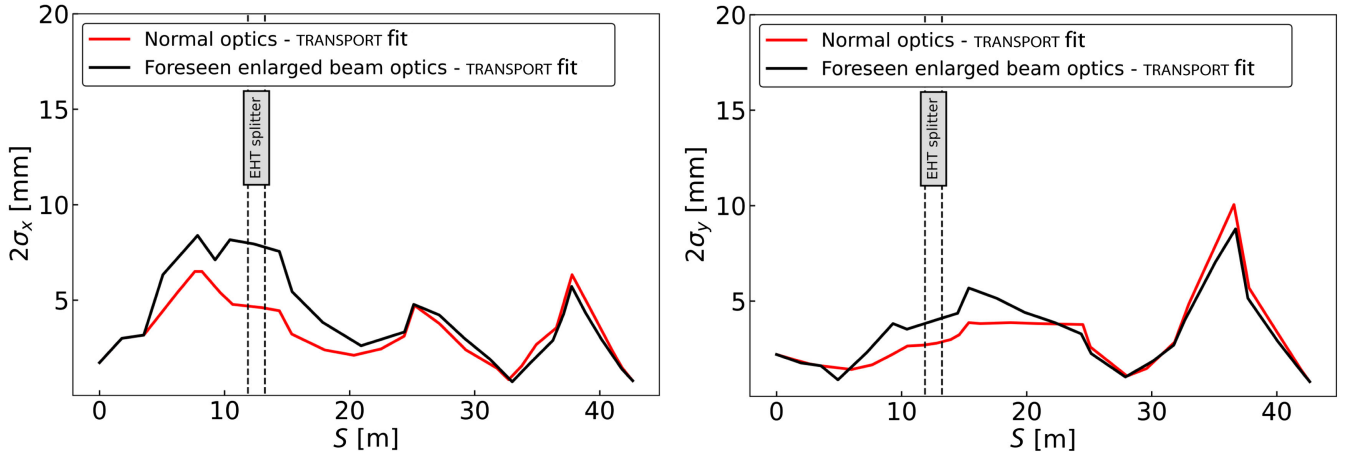

FIG. 12. 2σ horizontal (left) and vertical (right) TRANSPORT envelope fits from the upstream end of the AHA bending magnet to the entrance of target M for nominal and foreseen enlarged beam optics. The position of the EHT splitter is marked with dashed vertical lines.

A benchmarking campaign is undertaken to validate the simulation model against certain measured characteristics from the beam study described above.

A. Monte Carlo simulation

The aforementioned considerations led to the choice of BDSIM as the reference program for all calculations: BDSIM combines a suite of standard high energy physics codes (GEANT4, ROOT, and CLHEP) to create a computational model of an accelerator and its components [12]. In particular, the GEANT4 toolkit allows to probe the full range of physics processes. Notably, the hadron-nucleus interactions of interest (below 590 MeV incident proton energy) were characterized using the GEANT4 Bertini cascade model (*ftfp_bert*) which is most commonly used for high energy physics applications [15,30]. Furthermore, the physics list *"em ftfp_bert decay muon hadronic_elastic em_extra"* was chosen based on the recommendations from BDSIM/GEANT4 [31].

With regard to particle tracking, BDSIM includes a set of custom integrators that incorporate thick lens tracking routines using the Frenet-Serret coordinate system. These routines are typically only valid in the paraxial approximation. In the nonparaxial case, BDSIM resorts to a numerical integrator (typically fourth order Runge-Kutta). A full mathematical description of all BDSIM integrators is given in [31].

B. Geometrical construction and electric field definition

Implementing accurate and realistic geometric models of accelerator components is crucial for energy deposition calculations. As particles propagate through a given model, the interactions they undergo will depend on the materials and shapes of the constituent regions they travel through. On account of the already built-in geometry models in BDSIM, a hybrid approach [30] is undertaken whereby the magnetic elements in the PK1 beamline are created from predefined models, while for the more complex elements such as the EHT, a more focused approach is privileged. Indeed, BDSIM facilitates user-built elements of a wide range of geometrical forms and predefined materials from the GEANT4 NIST database.

All relevant geometrical features of the EHT may be implemented by first importing and converting its computer aided design (CAD) drawings (see Fig. 2) to tessellated solids based on the GEANT4 Geometry Description Markup Language (GDML) [32]. Using the recently developed Python library PYG4OMETRY [33], complex geometries may be converted in a few seconds and material composition assigned to each volume. Particular care must be taken to ensure that geometries do not overlap since this may lead to particles skipping geometries/volumes and generating errors in the final output. Integrating electromagnetic fields with user-built elements is a vital aspect in the simulation of the EHT. To this end, the electrostatic field of the EHT is

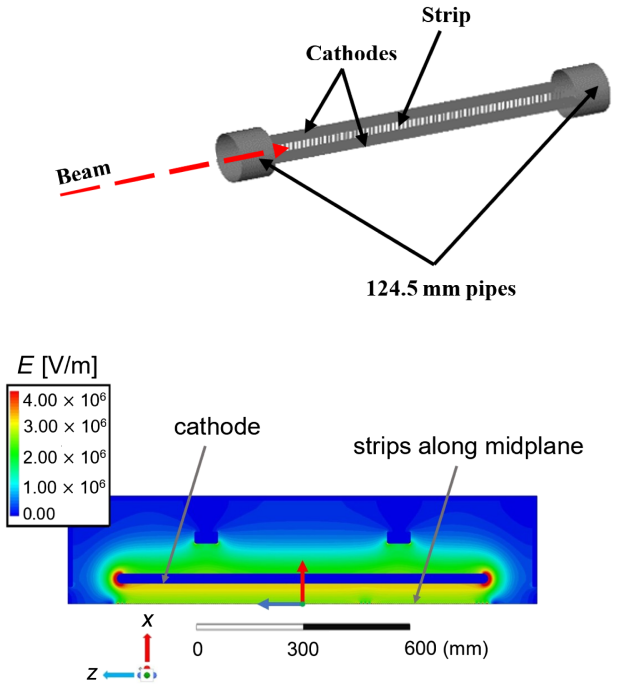

FIG. 13. Top: Simplified EHT geometry (GDML) implemented in BDSIM. Bottom: associated electrostatic field reflected on the upper horizontal middle plane. The beam direction is parallel to the z-direction forming a right-handed coordinate system. The strips follow the z-direction and are positioned along the axis of symmetry.

first simulated with ANSYS Maxwell [34]. Taking advantage of the symmetry of the EHT, the field simulation is performed with two mirror planes: x-z and y-z. A constant voltage of -172 kV is applied on both cathodes while 0 V is applied on the septum and vacuum chamber. In addition, an approximately uniform field is constructed between the tungsten strips and the two cathodes as well as a fringe field at the entrance and field fluctuations near the strips. The mesh is generated automatically and can be refined before the total number of tetrahedral elements reaches the program limit. This produces a complete 3D electric field map. Importantly, it is possible to further exploit symmetry and use a field map encompassing only a subset of the complete map. This approach effectively results in a reduction of loading time in BDSIM. The simplified EHT geometry as well as the associated electric field map in the upper horizontal plane is illustrated in Fig. 13. Finally, the PK1 beamline model is obtained by converting the TRANSPORT input files into BDSIM GMAD input [35] using a dedicated tool PYTRANSPORT. The 3D geometries (including the EHT) are then carefully placed one after another.

C. Beam description and beam optics considerations

BDSIM generates a given number of protons with (x, p_x, y, p_y, t, E) from an input Gaussian beam distribution where the standard deviation σ in each dimension as well as the

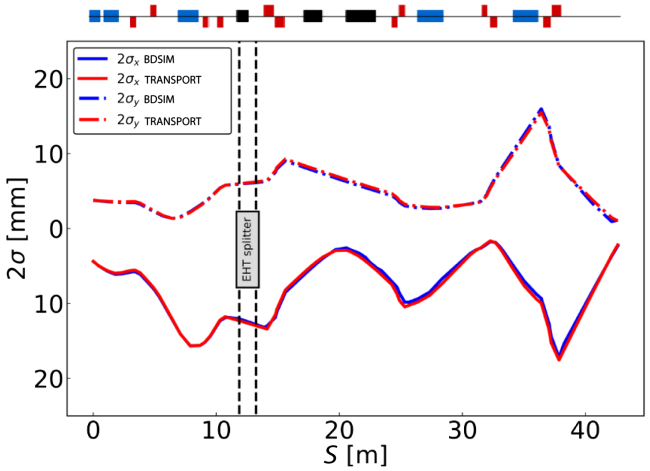

FIG. 14. Comparison of the beam envelopes between BDSIM and TRANSPORT for the tested second enlarged optics. The position of the EHT splitter is marked with dashed vertical lines.

off-diagonal correlation terms are specified in a 6×6 sigma matrix. As mentioned above, the TRANSPORT initial beam conditions for the three optics tested in our beam study are fed into BDSIM and tracking in magnetic fields is performed from the upstream end of the AHA bending magnet to the entrance of target M. In a BDSIM event, one proton is sampled from the initial beam distribution and tracked until reaching a termination condition (e.g., reaching zero kinetic energy or leaving the outermost "world" volume) [12]. Since simulating secondary particles are not required for validating the beam optics, no physics list is selected in BDSIM (i.e., particles pass unimpeded through matter). Comparison of the beam envelopes for the second enlarged case is shown in Fig. 14. A good agreement can be observed including in the critical region around the EHT, with the other two optics tested showing similar agreement. The schematic at the top of the figure depicts each magnet type in the accelerator (blue: dipoles, red: quadrupoles, black: collimator).

Finally, the measured main beam profiles, approximately 1.5 m upstream (profile monitors MHP5 and MHP6) of the EHT, are compared to the BDSIM profiles (Fig. 15).

In general, the agreement is quite satisfactory between simulations and measurements. However, some differences are present especially around the tails in both horizontal and vertical measurement distributions. Such asymmetries might reflect the direction of the wires of the wire scanner as they move into (respectively out) of the main beam distribution.

In the following section, the septum position of the EHT and its effect on the magnitude of split beam current are studied in BDSIM.

D. EHT septum position

In BDSIM, the beam center is set to $x = 0$ mm. The beam direction is parallel to the z direction forming a

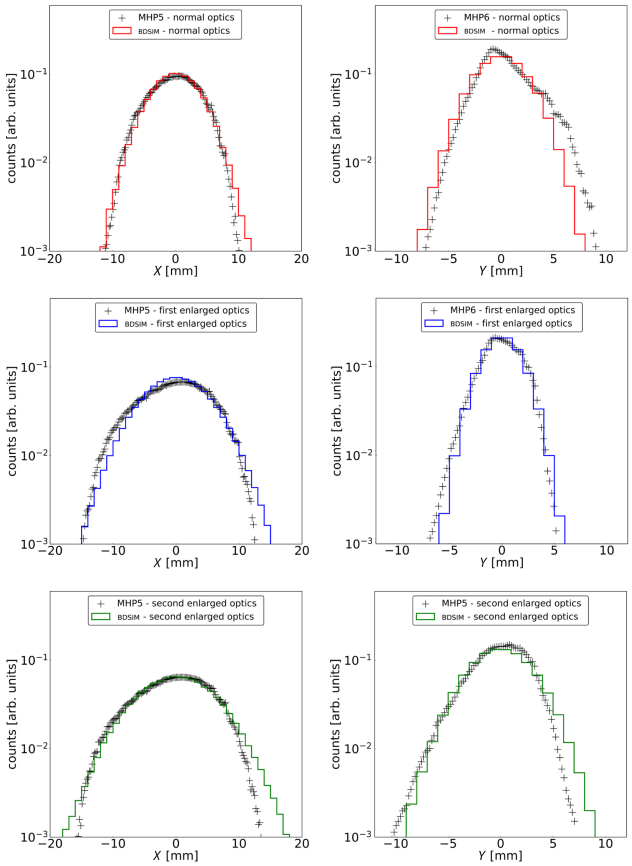

FIG. 15. Comparison of measured horizontal (left column) and vertical (right column) beam profiles (approximately 1.5 m upstream of the EHT) with BDSIM.

right-handed coordinate system. The simulation starts at the entrance of the EHT. Peeling off a portion of the main beam corresponds to shifting the center of the septum to a negative position x_0. Typically, for a standard deviation σ_x of the proton beam along the x axis, x_0 is approximately at $-1.95\sigma_x$ (assuming 50 μA peeled off from a 2-mA nominal beam). Having set this framework, the coordinates before and after the EHT may be recorded for each proton simulated. This allows to plot the horizontal phase space where the splitting of the main beam into two distinct bunches may be observed (Fig. 16). Importantly, the effect of shifting the septum position on the amount of split beam may also be noticed.

To find the position of the septum corresponding to the desired split intensity, one should solve numerically the following equation for x_0:

$$\int_{-\infty}^{x_0-\frac{1}{2}w} \frac{1}{\sqrt{2\pi\sigma_x^2}} e^{-\frac{x^2}{2\sigma_x^2}} dx = \frac{I}{I_0}, \tag{2}$$

where w is the width of the strip, σ_x is the one sigma standard deviation of the main beam distribution, I is the split beam intensity, and I_0 is the intensity of the main

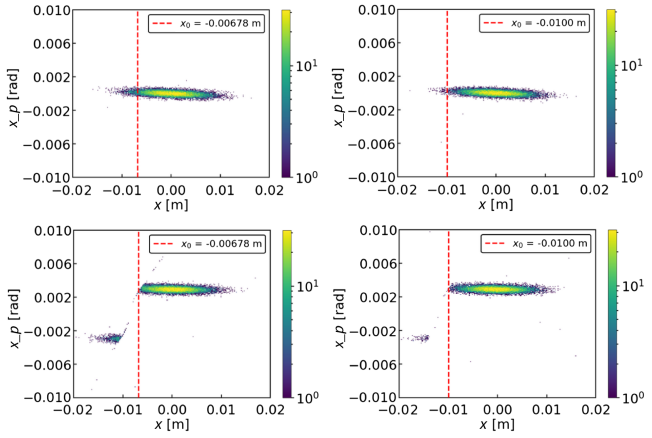

FIG. 16. Normal optics—horizontal phase space before (above) and after splitting (below) for different septum positions corresponding to 80 μA (left) and 10 μA (right) split current intensity, respectively.

beam. Furthermore using Eq. (2), the septum position may be calculated for several split currents (Fig. 17). This allows to retrieve the split beam profile (i.e., the tail of the initial Gaussian main beam distribution) for the three optics tested. As expected, for the normal optics, the split current is more sensitive to changes in the septum position. With regard to the stability of the EHT during operation, this provides an additional advantage for using enlarged beam optics.

Clearly, from Fig. 16, for a larger split current, the particle density on the strips of the EHT septum increases. As a consequence, the energy deposited can likewise increase drastically. This is studied via simulations in the following sections. Two solutions are studied to lower the power deposition on the strips, namely the rotation of the EHT in the horizontal plane and enlarging the beam optics in both planes.

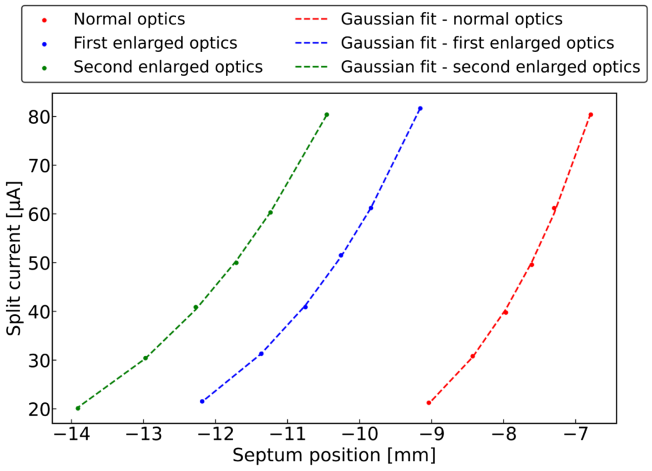

FIG. 17. EHT sensitivity curve—split current versus septum position.

E. EHT rotation angle

In order to have a power deposition as small as possible at the location of the septum, the EHT may be rotated in the horizontal plane. The optimal rotation angle corresponds to the average horizontal momentum at the location of the septum and can be found analytically as follows:

$$\theta_{\mathrm{opt}} = x_p + \frac{\sigma_{12}}{\sigma_{11}} \cdot x_0, \tag{3}$$

where x_p is the beam deflection, σ_{11} is the horizontal beam size (one Gaussian sigma) squared, σ_{12} is the correlation between the horizontal beamsize and angle, and x_0 is the position of the septum.

As an example, for a nominal beam with 50 μA split current, $\sigma_{12} = -0.238$ mm mrad, $x_0 = 7.607$ mm, and $\sigma_{11} = 15.264$ mm^2 at the entrance of the EHT giving $\theta_{\mathrm{opt}} = 0.118$ mrad. BDSIM allows to rotate an element by applying a transformation of the coordinate system before the rotation and reverting to it after the rotation. With these simulation tools, a parametric scan of the rotation angle was carried out to determine the angle that minimizes the power deposited on the EHT septum as a whole (Fig. 18). An optimal angle of $\theta_{\mathrm{opt}} = 0.12$ mrad is found validating Eq. (3).

F. Power deposition on first strip

With high energy protons like the ones extracted from the ring cyclotron, a very large number of secondary particles may be produced and lost. A loss point is the end of the trajectory of a primary proton due to inelastic collisions, fragmentation or absorption in matter. In BDSIM, the energy deposition is recorded in one- to three-dimensional histograms made on an event-by-event basis or as a simple integration across all events. Accordingly, the power deposition on the first three strips of the EHT may be

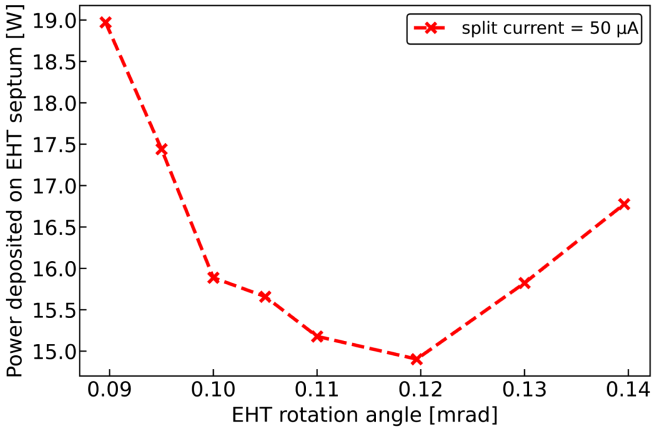

FIG. 18. Total power deposited from simulated primary and secondary particles on the EHT septum as a function of its rotation angle. Normal optics case with 50 μA split current is shown.

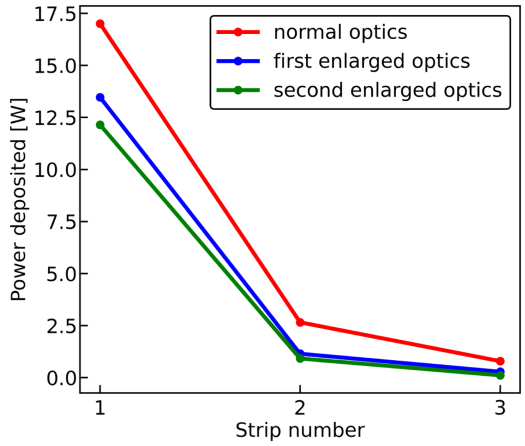

FIG. 19. Power deposited on the first three strips for 100 μA split current for the three different optics.

calculated for the three optics tested (Fig. 19). As can be seen, the power deposited is most significant on the first strip and negligible from the third onward.

In light of this, an analytical model predicting the power deposited on the first strip was set up with the following considerations. Assuming a 2 mA proton beam current extracted from the ring cyclotron, the proton rate is given by

$$\mathrm{R_p} = \frac{I}{e} = 1.25 \times 10^{16}\ \mathrm{s}^{-1}, \tag{4}$$

where I is the beam current from the ring cyclotron and e is the elementary charge.

For a given split current and beam size, the proton rate interacting with the EHT septum is computed as

$$R_p^{\mathrm{septum}} = R_p \cdot \int_{x_0-\frac{w}{2}}^{x_0+\frac{w}{2}} \frac{1}{\sqrt{2\pi\sigma_x^2}} e^{\frac{-x^2}{2\sigma_x^2}} dx, \tag{5}$$

where x_0 is the septum position, w is the width of the strip, and σ_x is the one sigma standard deviation of the main beam distribution. In addition, the energy lost by a 590 MeV proton in 2 mm (length of a strip, Δz) of tungsten is given by the Bethe-Bloch formula [36] approximated with finite differences:

$$E_{\mathrm{dep}} = -\langle \Delta E \rangle \approx \frac{4\pi}{m_e c^2} \cdot \frac{nz^2}{\beta^2} \cdot \left(\frac{e^2}{4\pi\varepsilon_0^2}\right)^2 \cdot \left[\ln\left(\frac{2m_e c^2\beta^2}{I\cdot(1-\beta^2)}\right) - \beta^2\right] \Delta z. \tag{6}$$

The power deposited on a strip is then $P_{\mathrm{dep}} = R_p^{\mathrm{septum}} \cdot E_{\mathrm{dep}}$. Using this procedure, the analytical power deposited on the first strip is compared for all three optics to the simulated power deposition. In BDSIM, two power deposition calculations are made: one involving only primary particles and another considering both primary and secondary particles (Fig. 20). The optimal rotation angle is also taken into consideration.

When primary particles are exclusively simulated, the BDSIM results show a good agreement with the analytical model. This is expected since both of these calculations do not consider nuclear processes. When secondary particles are also taken into account in the simulation, the total power deposited on the first strip is the sum of the power depositions from both primary and secondary particles.

V. CONCLUSION

A successful beam study was carried out where a record 90 μA, corresponding to 53 kW beam power, was peeled off by the EHT electrostatic beam splitter and sent to the UCN target. To reach such high split beam intensity and power (while also maximizing the stability of the peeled beam), the EHT was operated with a horizontally and vertically enlarged beam. Diagnostic power deposition measurements carried out during the beam study were validated with a dedicated Monte Carlo simulation tool, BDSIM. Both measurements and simulation show that an enlarged beam optics is beneficial to reduce not only the

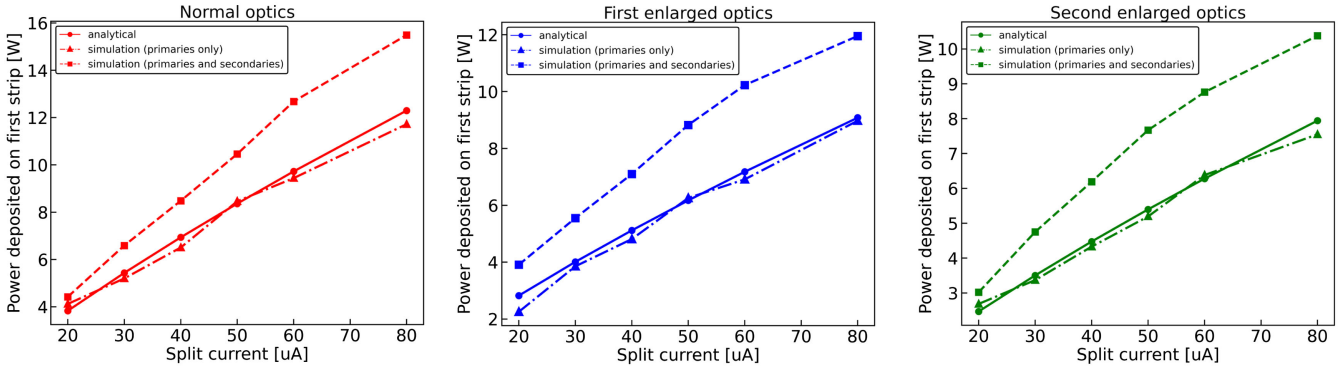

FIG. 20. Power deposited on first strip versus split current—analytical model versus BDSIM simulations with primary particles only (dotted dashed line) and with both primary and secondary particles (dashed line).

power deposited on the strips of the EHT but also the beam losses a few meters downstream in the PK1 beamline. In addition, several properties of the EHT were studied in detail through simulations, including optimizing certain parameters like the rotation angle to minimize the high-power deposition on the EHT strips. Likewise, benchmarking BDSIM/GEANT4 simulations with the beam profile measurements and beam envelopes further confirmed the accuracy of Monte Carlo simulation tools. Radiation damage and activation studies are ongoing to estimate the lifetime of the EHT. Finally, beam studies with water cooled quadrupoles are planned and will allow to test more enlarged beam optics and to reach higher split beam intensities. With such improvements, we are confident that the existing EHT can be used to operate at 100 μA for TATTOOS.

[1] J. Grillenberger, C. Baumgarten, and M. Seidel, SciPost Phys. Proc. **5**, 002 (2021), https://scipost.org/SciPostPhysProc.5.002.

[2] D. Reggiani, in *Proceedings of the 52nd ICFA Advanced Beam Dynamics Workshop on High-Intensity and High-Brightness Hadron Beams, HB2012, Beijing, China* (JACoW, Geneva, Switzerland, 2013), pp. 373–377.

[3] D. Kiselev, P.-A. Duperrex, S. Jollet, S. Joray, D. Laube, D. Reggiani, R. Sobbia, and V. Talanov, SciPost Phys. Proc. **3**, 003 (2021), https://scipost.org/SciPostPhysProc.5.003.

[4] N. van der Meulen *et al.*, in *Proceedings of 22nd International Conference on Cyclotrons and their Applications, CYC2019, Cape Town, South Africa* (JACoW, Geneva, Switzerland, 2020), TUA03, https://doi.org/10.18429/JACoW-Cyclotrons2019-TUA03.

[5] M. Olivo and H. V. Reist, in *Proceedings of the First European Particle Accelerator Conference, EPAC1988, Rome, Italy* (JACoW, Geneva, Switzerland, 1988), pp. 1300–1303.

[6] H. Zhang *et al.*, in *Proceedings of the 22nd International Conference on Cyclotrons and their Applications, CYC2019, Cape Town, South Africa* (JACoW, Geneva, Switzerland, 2020), WEB04, https://doi.org/10.18429/JACoW-Cyclotrons2019-WEB04.

[7] M. Olivo, U. Rohrer, and E. Steiner, IEEE Trans. Nucl. Sci. **28**, 3094 (1981).

[8] E. Mariani, M. Olivo, and D. Rossetti, in *Proceedings of the 6th European Particle Accelerator Conference, Stockholm, 1998* (IOP, London, 1998), pp. 2129–2131.

[9] R. Eichler *et al.*, Paul Scherrer Institut, Villigen PSI, Switzerland, Report No. 22-01, 2022, https://www.dora.lib4ri.ch/psi/islandora/object/psi:41209.

[10] PSI, TATTOOS description, https://www.psi.ch/en/impact/tattoos (2022).

[11] M. Hartmann, D. Kiselev, D. Reggiani, J. Snuverink, H. Zhang, and M. Seidel, J. Phys. Conf. Ser. **2420**, 012105 (2023).

[12] L. Nevay, S. Boogert, J. Snuverink, A. Abramov, L. Deacon, H. Garcia-Morales, H. Lefebvre, S. Gibson, R. Kwee-Hinzmann, W. Shields *et al.*, Comput. Phys. Commun. **252**, 107200 (2020).

[13] S. Agostinelli, J. Allison, K. A. Amako, J. Apostolakis, H. Araujo, P. Arce, M. Asai, D. Axen, S. Banerjee, G. Barrand *et al.*, Nucl. Instrum. Methods Phys. Res., Sect. A **506**, 250 (2003).

[14] J. Allison *et al.*, IEEE Trans. Nucl. Sci. **53**, 270 (2006).

[15] J. Allison *et al.*, Nucl. Instrum. Methods Phys. Res., Sect. A **835**, 186 (2016).

[16] M. Seidel *et al.*, Conf. Proc. C **100523**, TUYRA03 (2010), https://inspirehep.net/literature/870002.

[17] M. J. Barnes, J. Borburgh, B. Goddard, and M. Hourican, in *CERN Accelerator School: Course on Magnets* (2011).

[18] U. Rohrer, Paul Scherrer Institute, Technical Report No. INIS-CH-012, 1999, pp. 14–15, https://www.osti.gov/etdeweb/biblio/10147456.

[19] H. Banderier, Paul Scherrer Institute, Technical Report No. THESIS 000123, 2020.

[20] J. Weber, Paul Scherrer Institute, Technical Report No. THESIS 000124, 2021.

[21] D. Reggiani *et al.*, in *Proceedings of DIPAC'11* (JACoW, Geneva, Switzerland, 2011), pp. 35–37.

[22] D. Anicic, M. Daum, G. Dzieglewski, D. George, M. Horvat, G. Janser, F. Jenni, I. Jirousek, K. Kirch, T. Korhonen *et al.*, Nucl. Instrum. Methods Phys. Res., Sect. A **541**, 598 (2005).

[23] K. L. Brown, F. Rothacker, D. C. Carey, and C. Iselin, European Organization for Nuclear Research, Technical Report No. CERN-80-04, 1980, https://cds.cern.ch/record/133647.

[24] U. Rohrer, graphic transport/turtle framework, http://aea.web.psi.ch/Urs_Rohrer/MyWeb.

[25] T. Stammbach, S. Adam, T. Blumer, D. George, A. Mezger, P. Schmelzbach, and P. Sigg, AIP Conf. Proc. **600**, 423 (2001).

[26] R. Baartman, in *Proceedings of the 20th International Conference on Cyclotrons and their Applications, Vancouver, Canada* (2013), pp. 16–20.

[27] P. Bertrand and C. Ricaud, AIP Conf. Proc. **600**, 379 (2001).

[28] A. Kolano, A. Adelmann, R. Barlow, and C. Baumgarten, Nucl. Instrum. Methods Phys. Res., Sect. A **885**, 54 (2018).

[29] H. Zhang (private communication).

[30] M. H. Tahar, D. Kiselev, A. Knecht, D. Laube, D. Reggiani, and J. Snuverink, Nucl. Instrum. Methods Phys. Res., Sect. A **1046**, 167638 (2022).

[31] BDSIM Manual, http://www.pp.rhul.ac.uk/bdsim/manual (2023).

[32] GDML description website, https://gdml.web.cern.ch/GDML/ (2022).

[33] S. Walker, A. Abramov, L. Nevay, W. Shields, and S. Boogert, Comput. Phys. Commun. **272**, 108228 (2022).

[34] ANSYS Maxwell, https://www.ansys.com/products/electronics/ansys-maxwell.

[35] I. Agapov, EUROTev, Technical Report, No. EUROTEV-MEMO-2006-003-1, 2006, http://cds.cern.ch/record/972077?ln=en.

[36] J. D. Cockcroft, Nature (London) **175**, 53 (1955).